The Astrophysical Journal, 990:57 (11pp), 2025 September 1 https://doi.org/10.3847/1538-4357/adee91
© 2025. The Author(s). Published by the American Astronomical Society.
OPEN ACCESS

# JWST Discovery of Warm Dust in the Circumgalactic Medium of the Makani Galaxy

Sylvain Veilleux[1,2], Steven D. Shockley[1], Marcio Meléndez[3], David S. N. Rupke[4,5], Alison L. Coil[6], Aleksandar M. Diamond-Stanic[7], James E. Geach[8], Ryan C. Hickox[9], John Moustakas[10], Gregory H. Rudnick[11], Paul H. Sell[12], Christy A. Tremonti[13], and Hojoon Cha[13]
[1] Department of Astronomy, University of Maryland, College Park, MD 20742, USA
[2] Joint Space-Science Institute, University of Maryland, College Park, MD 20742, USA
[3] Space Telescope Science Institute, Baltimore, MD 21218, USA
[4] Department of Physics, Rhodes College, Memphis, TN 38112, USA
[5] Zentrum für Astronomie der Universität Heidelberg, Astronomisches Rechen-Institut, Münchhofstr. 12-14, D-69120 Heidelberg, Germany
[6] Department of Astronomy and Astrophysics, University of California, La Jolla, CA 92092, USA
[7] Department of Physics and Astronony, Bates College, Lewiston, ME 04240, USA
[8] Centre for Astrophysics Research, Department of Physics, Astronomy and Mathematics, University of Hertfordshire, Hatfield, AL10 9AB, UK
[9] Department of Physics and Astronomy, Dartmouth College, Hanover, NH 03755, USA
[10] Department of Physics and Astronomy, Siena College, 515 Loudon Rd., Loudonville, NY 12110, USA
[11] Department of Physics and Astronomy, University of Kansas, Lawrence, KS 66045, USA
[12] Department of Astronomy, University of Florida, Gainesville, FL 32611, USA
[13] Department of Astronomy, University of Wisconsin–Madison, Madison, WI 53706, USA
*Received 2025 May 1; revised 2025 June 15; accepted 2025 July 10; published 2025 August 25*

## Abstract

We report the detection of near- and mid-infrared emission from polycyclic aromatic hydrocarbons (PAHs) out to ∼35 kpc in the Makani Galaxy, a compact massive galaxy with a record-breaking 100 kpc scale starburst-driven wind at redshift $z = 0.459$. The NIRCam and MIRI observations with JWST take advantage of a coincidental match between the PAH spectral features at 3.3, 7.7, and (11.3 + 12.2) $\mu$m in Makani and the bandpasses of the MIRI and NIRCam filters. The warm dust is not only detected in the cool-gas tracers of the galactic wind associated with the more recent (7 Myr) starburst episode, but also in the outer warm ionized gas wind produced by the older (0.4 Gyr) episode. The presence of PAHs in the outer wind indicates that the PAHs have survived the long ($R/v \sim 10^8$ yr) journey to the halo despite the harsh environment of the galactic wind. The measured F1800W/F1130W flux ratios in the unresolved nucleus, inner halo ($R$ = 10–20 kpc), and outer halo ($R$ = 20–35 kpc), tracers of the PAH (11.3 + 12.2)/7.7 ratios, indicate decreasing starlight intensity incident on the PAHs, decreasing PAH sizes, and increasing PAH ionization fractions with increasing distance from the nucleus. These data provide the strongest evidence to date that the ejected dust of galactic winds survives the long journey to the circumgalactic medium, but is eroded along the way.

*Unified Astronomy Thesaurus concepts:* Galactic winds (572); Stellar feedback (1602); Starburst galaxies (1570); Circumgalactic medium (1879); Shocks (2086); Dust physics (2229)

## 1. Introduction

The amount of dust outside galaxies, inferred from reddening measurements of background quasars and galaxies by foreground galaxy halos (B. Ménard et al. 2010; J. E. G. Peek et al. 2015; J. E. McCleary et al. 2025), is comparable to that within galaxies, but the origin of this dust is uncertain (e.g., J. Tumlinson et al. 2017; C.-A. Faucher-Giguère & S. P. Oh 2023; and references therein). Sophisticated cosmological galaxy formation simulations (e.g., M. Vogelsberger et al. 2014; J. Schaye et al. 2015; Y. Dubois et al. 2016; P. Biernacki & R. Teyssier 2018; R. Brennan et al. 2018; E. Choi et al. 2018; P. F. Hopkins et al. 2018; R. Davé et al. 2019; Z. Hafen et al. 2019; D. Nelson et al. 2019; M. S. Peeples et al. 2019; D. Narayanan et al. 2023) suggest that galactic winds, driven by stellar or supermassive black hole processes, are the primary source of the enriched circumgalactic medium (CGM), but the direct detection of dust in a galactic wind on the relevant CGM scale remains elusive (e.g., S. Veilleux et al. 2020 and references therein).

Original content from this work may be used under the terms of the Creative Commons Attribution 4.0 licence. Any further distribution of this work must maintain attribution to the author(s) and the title of the work, journal citation and DOI.

The recently discovered 100 kpc scale wind in the Makani Galaxy (SDSS J211824.06+001729.4; D. S. N. Rupke et al. 2019), a massive ($M_* = 10^{11.1}\,M_\odot$) but compact ($r_e = 2.3$ kpc) poststarburst galaxy at $z = 0.459$ (P. H. Sell et al. 2014), is an excellent target for testing this idea. The cooler neutral-atomic and molecular gas phases in this wind coexist with the warm ionized gas to distances of ∼20 kpc but apparently not beyond. This provides tantalizing evidence that we are witnessing, for the first time on the CGM scale, the dissolution of the outflowing cool clouds into the warm ionized phase as theoretically predicted (e.g., E. Scannapieco & M. Brüggen 2015; A. Ferrara & E. Scannapieco 2016; D. Decataldo et al. 2017). The lack of significant reddening in the warm ionized gas beyond the cool molecular/neutral-atomic gas (based on the long-slit measurements of the H$\alpha$/H$\beta$ emission line ratio from D. S. N. Rupke et al. 2023) further suggests that dust does not survive the journey beyond ∼25 kpc.

The exquisite infrared sensitivity and image quality of JWST provide new tools to examine this issue. Indeed several MIRI and NIRCam filters (J. P. Gardner et al. 2023; J. Rigby et al. 2023) are specifically designed to capture key spectral features from warm dust (PAH 3.3, 7.7, 11.2, and 17.0) and molecular gas ($H_2$ 0–0 S(1) 17.03). Multiband NIRCam and MIRI images of the classic starburst galaxy M82 have beautifully demonstrated the

ability of JWST to map polycyclic aromatic hydrocarbons (PAHs) in nearby galactic wind systems (A. D. Bolatto et al. 2024; D. B. Fisher et al. 2025). However, these PAH features are redshifted out of the filter bandpasses in galaxies with $z \gtrsim 0.03$. The Makani Galaxy is a remarkable exception: at $z = 0.459$, the bandpasses of seven MIRI and NIRCam filters coincide with redshifted Pa$\beta$, PAH 3.3, PAH 7.7, (PAH 11.3 + 12.7), (PAH 17.0 + $H_2$ S(1) 17.03), and two largely featureless continuum windows (Figure 1). Observations through these filters therefore offer a unique window on the warm dust, $H_2$, and ionized gas content across the entire galactic wind of Makani.

This paper reports the results of our analysis of the multifilter MIRI and NIRCam data on Makani obtained by our group on 2023 June 30 (PID GO-1865, PI: Veilleux). These data are publicly available on the Mikulski Archive for Space Telescopes (MAST) at the Space Telescope Science Institute. The specific observations analyzed can be accessed via doi:10.17909/1r37-nb46. Section 2 briefly describes the observing strategy and MIRI and NIRCam observations. The results from our analysis are presented in Section 3 and the implications of these results on the issues of dust survival and evolution are discussed in Section 4. The conclusions are summarized in Section 5. Throughout this paper, we take as systemic the stellar redshift of Makani, $z = 0.4590$ (D. S. N. Rupke et al. 2019) and assume a flat $\Lambda$ cosmology with $\Omega_m = 0.315$ and $H_0 = 67.4$ km s$^{-1}$ Mpc$^{-1}$ (Planck Collaboration et al. 2020), resulting in a projected physical scale of 6.02 kpc arcsec$^{-1}$ at the distance of Makani.

## 2. Observations

### 2.1. Observing Strategy

Makani is at a very convenient redshift: the bandpass of F480M is centered on redshifted PAH 3.3 $\mu$m, F1130W on redshifted PAH 7.7 $\mu$m, F1800W on redshifted PAH (11.3 + 12.2) $\mu$m, and F2550W on redshifted $H_2$ 17.03 $\mu$m, while F770W and F2100W cover the largely featureless continuum emission at rest-frame 4.5–6 $\mu$m and 13–16 $\mu$m, respectively (Table 1, Figure 1). Moreover, F187N, which comes for free while observing with F480M, also happens to be centered on redshifted Pa$\beta$. The flux measurements from F770W and F2100W constrain the strength and slope of the continuum emission without PAH contamination. They can therefore be used in principle as "off-band" filters to estimate the continuum-subtracted fluxes of the PAH 3.3, 7.7, (11.3 + 12.2), and $H_2$ 17.03 features. Some weaker features contaminate our measurements (column (3) in Table 1), but their contributions are negligibly small (this is discussed in Section 3.2 below).

### 2.2. MIRI Observations

The MIRI exposures were broken into short segments to avoid saturation on the central galaxy core. For all observations, the recommended default readout mode for imaging, FAST, and a four-point extended-source dither pattern were used. The F770W, F1130W, and F1800W observations were respectively split into 60 groups, one integration, and 12 exposures; 35 groups, one integration, and 16 exposures; and 30 groups, one integration, and 20 exposures, keeping the integration time at each dither position below 1000 s. For the long-wavelength F2100W and F2550W observations, the maximum dwell time at each dither position was kept well below 8 minutes using 28 groups, one integration, and 36 exposures, and 20 groups, one integration, and 64 exposures, respectively. The MIRI FULL array field of view (FOV; $74'' \times 114''$) is large enough to cover the full extent of Makani and provides source-free sky beyond the galactic wind, so separate background observations were not requested.

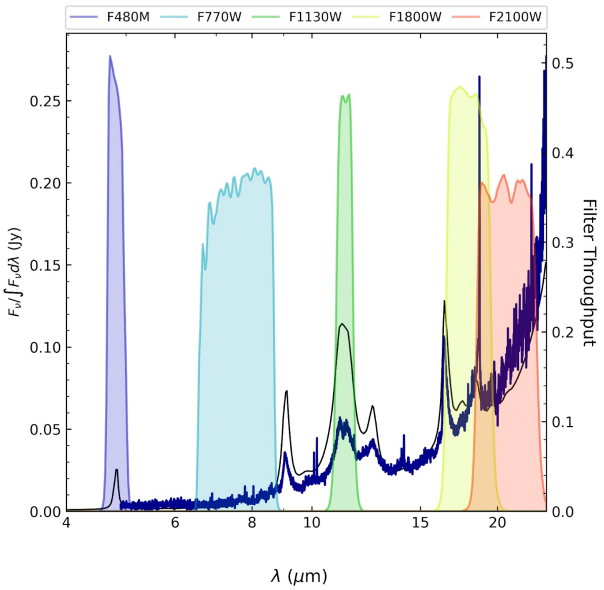


**Figure 1.** The transmission curves of both the NIRCam and MIRI filters are overlaid on the nuclear spectrum of Makani (from A. Erena et al. 2025, in preparation; thick line) and one of the model spectra of B. T. Draine et al. (2021; thin line). The wavelength is in the observer's frame. The left axis shows the normalized spectral intensity and the right axis indicates the filter throughput. Several filters are centered on distinct PAH features while others cover the featureless continuum. Non-PAH features, such as fine-structure atomic lines, contaminate the fluxes within some filters, but their overall contributions can safely be ignored. See column (3) in Table 1 and Section 3.2 for more details.

**Table 1**
NIRCam and MIRI Observations

| Filters | Main Diagnostics | Weaker Feature(s) | $t_{exp}$ (hr) |
|---|---|---|---|
| (1) | (2) | (3) | (4) |
| N-F187N | Pa$\beta$ 1.28 | ⋯ | 0.90 |
| N-F480M | PAH 3.3 | ⋯ | 0.90 |
| M-F770W | Continuum (5 $\mu$m) | ⋯ | 0.56 |
| M-F1130W | PAH 7.7 | ⋯ | 0.44 |
| M-F1800W | PAH (11.3 + 12.2) | [Ne II] 12.8 | 0.47 |
| M-F2100W | Continuum (14 $\mu$m) | [Ne II] 12.8 + [Ne III] 15.5 | 0.78 |
| M-F2550W | $H_2$ 17.03 | PAH 17.0 | 1.00 |

**Note.** Meaning of the columns: (1) Name of the NIRCam (N) or MIRI (M) filters. (2) Main diagnostics in the filter bandpass. (3) Weaker feature(s) in the filter bandpass. (4) On-target exposure in hours (excluding overheads).

### 2.3. NIRCam Observations

A similar strategy was used for the NIRCam F480M observations. To reach a good signal-to-noise ratio (S/N) in the wind, avoid saturation on the galaxy, and reduce overheads and data volume, an on-target exposure time of 1 hr was split into 10 groups, one integration, and 20 exposures using the

MEDIUM8 readout pattern and subarray SUB400P. This number of groups mitigates cosmic rays for all pixels and maximizes S/N while keeping the integration times per exposure well below 1000 s, as recommended. The recommended larger subpixel STANDARD dithers were used to better mitigate bad pixels in the case where no primary dithers were performed. Separate background observations were not requested since the FOV of the SUB400P subarray of the long-wavelength side of NIRCam (25.″0 × 25.″0) is large enough to cover the full extent of Makani and provide source-free sky beyond the wind. The FOV on the short-wavelength side of NIRCam (12.″4 × 12.″4) covers most of the [O II] galactic wind and some source-free sky along the short axis of the wind.

## 3. Results

### 3.1. Data Reduction and Analysis

All data used for this analysis were processed using the JWST calibration pipeline version 1.10.1. We used the dither-combined stage 3 products (i2d fits) from the Mikulski Archive for Space Telescopes (MAST).

We are interested in the faint extended emission outside of the bright central starburst of Makani. Therefore, we need to carefully remove the bright central point-spread function (PSF). To model the JWST PSF, we employed STPSF (version 2.0.0; M. D. Perrin et al. 2014), a Python package that leverages in-flight wave front measurements to simulate the observed PSFs taking into account detector pixel scales, rotations, filter profiles, and detector effects. Note that STPSF incorporates simplified models for detector effects like interpixel capacitance, charge diffusion, and the MIRI cruciform artifact. While the current model accounts for field dependence in the cruciform artifact, discrepancies between predicted and observed flux persist.

We modeled the optimal PSF for our 2023 June 30 Makani observations using the closest-in-time optical path difference map. These wave front measurements, regularly available on MAST, enable STPSF to generate time-dependent PSFs that accurately reflect the telescope's optical performance at the time of the science observations. Subsequently, we utilized the `PSFPhotometry` module from the `photutils` Python package to create residual images. This involved fitting and subtracting our STPSF PSF model from the Makani observations at each wavelength.

### 3.2. Continuum and Emission Line Contamination

The stellar continuum from the galaxy is negligible beyond $r \simeq 1''$ (6 kpc) from the center of this compact galaxy ($r_{1/2}$ = 2.3 kpc; P. H. Sell et al. 2014). However, some fine-structure lines may contaminate our measurements (column (3) in Table 1, Figure 1): [Ne II] 12.8 in F1800W and both [Ne II] 12.8 and [Ne III] 15.5 in F2100W (we ignore the PAH 17.0 + $H_2$ blend in F2550W since no extended emission is detected in this filter). This flux correction is only ∼1% in the nuclear spectrum of Makani (Figure 1) and typically less than 5% of the PAH (11.3 + 12.2) flux in the wind of M82 (P. Beirão et al. 2015; A. D. Bolatto et al. 2024). Similarly, the [Ne III] contribution to the rest-frame 14 $\mu$m continuum emission in the F2100W filter is less than 1% in the nuclear spectrum of Makani and <5% assuming [Ne III] 15.5 / [Ne II] 12.8 $\simeq 1/3$ (e.g., M82 wind: P. Beirão et al. 2015). Both [Ne II] and [Ne III] therefore contribute negligibly to the measured fluxes in filters F1800W and F2100W; they are ignored in the remainder of our discussion.

### 3.3. Distribution of the Warm Dust Relative to the Cool and Warm Gas Phases

The results from the PSF subtraction with STPSF are shown in Figures 2−4. To help assess the full extent of the extended emission associated with Makani, we directly compare the PSF-subtracted MIRI and NIRCam images of Makani with the Hubble Space Telescope (HST) F814W (stellar continuum near ∼6000 Å in the rest frame), Atacama Large Millimeter/submillimeter Array (ALMA) CO (2–1), KCWI Mg II 2800 Å, and KCWI [O II] 3727 Å flux maps from D. S. N. Rupke et al. (2019). The blue circles in these figures identify possible galaxies in the field. Figures 2 and 3 show that warm dust is clearly detected beyond the inner cold molecular gas traced by CO (2−1) and the inner cool neutral-atomic gas traced by Mg II (ionization potential (IP) = 8 eV), respectively. On the other hand, Figure 4 shows that the mid-infrared emission is less extended than the warm ionized gas traced by [O II]. Not shown in these figures is the fact that the redshifted PAH 17.0 + $H_2$ 17.03 blend and underlying continuum emission probed by the F2550W filter remains undetected beyond ∼1″ due to the lower-than-expected sensitivity of MIRI at 25 $\mu$m and the contaminating emission from the central unresolved galaxy, which is not only more extended at these long wavelengths due to the wavelength dependence of the diffraction pattern but also brighter (Figure 1). Similarly, the F187N image, which came for free with the F480M observations, is too shallow to reveal extended redshifted Pa$\beta$ line emission beyond ∼1″. The F187N and F2550W observations are not discussed any further in this paper.

In Figure 5, we compare the azimuthally averaged surface brightness radial profiles of [O II], Mg II, and CO 2−1 from D. S. N. Rupke et al. (2019, 2023) with the PAH emission at 3.3, 7.7, and (11.3 + 12.2) derived from the NIRCam and MIRI PSF-subtracted images shown in Figures 2−4. This figure highlights the detection of extended warm dust emission in the images of F1130W (rest-frame PAH 7.7 $\mu$m) and F1800W (rest-frame PAH 11.3 + 12.2 $\mu$m), and to a lesser extent in the images of F480M (rest-frame PAH 3.3 $\mu$m) and F770W (rest-frame continuum 5 $\mu$m), well beyond the CO 2–1 and Mg II line emission, which is not detected beyond ∼20 kpc. Note, however, that the F1130W/CO (2−1), F1800W/CO (2−1), F1130W/Mg II, and F1800W/Mg II flux ratios remain relatively constant out to 20 kpc. We discuss the physical implications of these results in Section 4.

In addition, clear asymmetries in the mid-infrared emission are visible in Figures 2−4, but are not captured in the azimuthally averaged radial profiles shown in Figure 5. In particular, a cloud complex is visible in the outer halo of the PSF-subtracted F1130W and F1800W images, extending out to 30–35 kpc NW of the galaxy nucleus. The (upper limits on the) flux densities measured within two circular apertures that encompass these clouds are listed in Table 2 (the footprints of these apertures are shown in red in Figure 6). For comparison, we also measure the fluxes in the nucleus and the inner halo, defined as the annular region centered on the nucleus with inner and outer radii of 1.″78 (10.5 kpc) and 3″ (17.6 kpc), respectively, shown in purple in Figure 6. The variations in the flux ratios within the various apertures are discussed in Section 4.

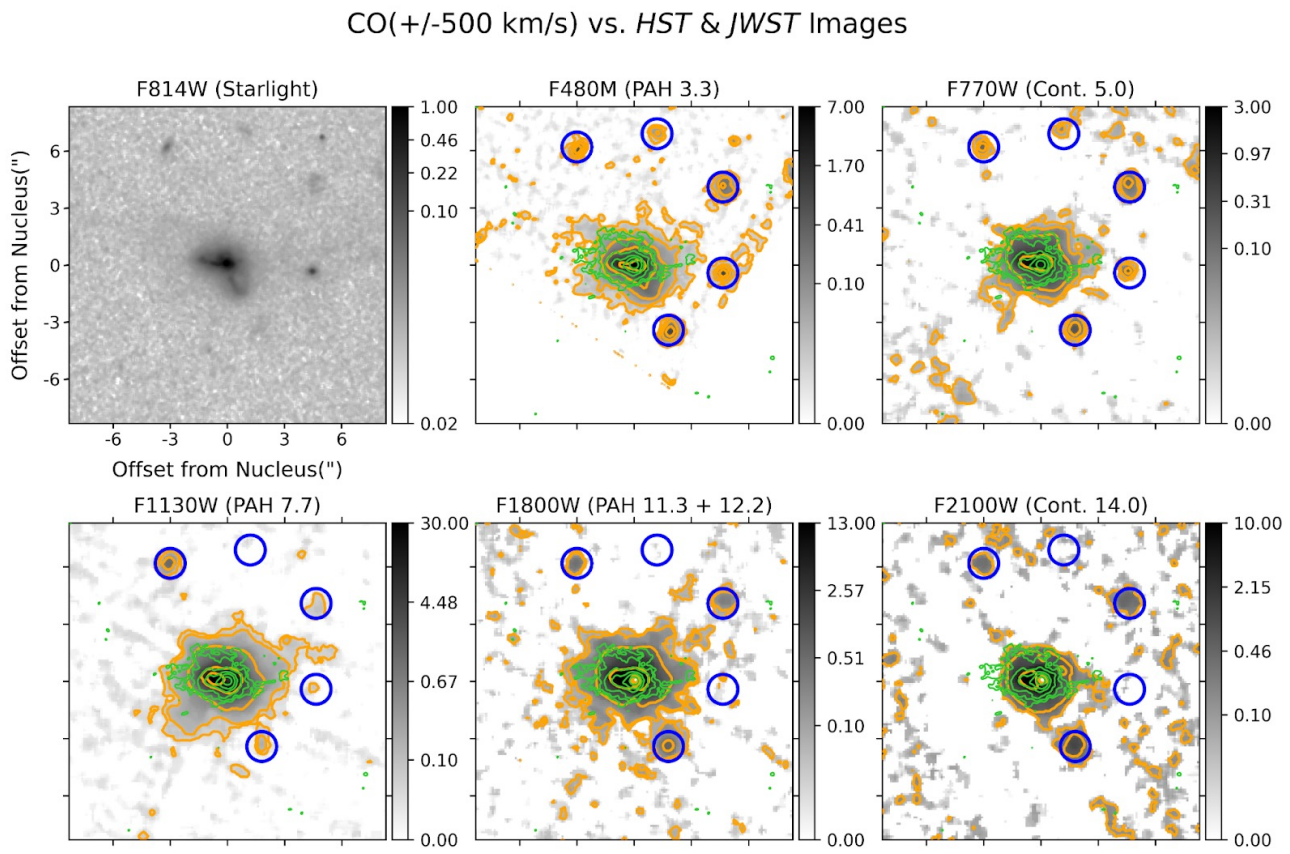


**Figure 2.** The top-left panel shows the stellar emission of Makani at rest-frame ∼5600 Å mapped in the HST F814W filter. The gray scale for that panel is in counts $s^{-1}$ $pixel^{-1}$. The other panels show the flux maps of the dust emission (orange contours) in the JWST NIRCam F480M and MIRI F770W, F1130W, F1800W, and F2100W filters after PSF subtraction with STPSF. The FOV of each panel is approximately 100 × 100 kpc. The gray scale for the JWST data is in units of MJy $sr^{-1}$. The orange contour levels are 0.01, 0.03, 0.1, 0.3, and 3.0 MJy $sr^{-1}$ for F480M, 0.01, 0.03, 0.1, and 1.0 MJy $sr^{-1}$ for F770W, 0.05, 0.1, 0.5, 5.0, and 15.0 MJy $sr^{-1}$ for F1130W, 0.05, 0.1, 0.5, and 5.0 MJy $sr^{-1}$ for F1800W, and 0.1, 0.5, and 5.0 MJy $sr^{-1}$ for F2550W. The CO (2–1) line emission within [−500, +500] km $s^{-1}$ from D. S. N. Rupke et al. (2019) is shown for comparison as green contours, where the contour levels are 0.09, 0.14, 0.28, 0.5, 0.8, and 1.2 mJy $beam^{-1}$. The blue circles identify possible galaxies in the field.

## 4. Discussion

Here we discuss the implications of the JWST results on the issue of dust survival in the circumgalactic environment (Section 4.1) and how dust evolves as it is carried away by the wind to these large distances (Section 4.2).

### 4.1. Warm Dust in the Outer Wind of Makani

The spatially resolved [O II] kinematics derived from the KCWI data cube in D. S. N. Rupke et al. (2019) cleanly separate the wind into an outer region ($r$ = 20–50 kpc) made up of warm ionized gas with maximum blueshifted velocities ($v_{98\%}$) between −100 and −700 km $s^{-1}$ and an inner region ($r \lesssim 20$ kpc) where the warm ionized gas traced by [O II] has a high-velocity tail to −2100 km $s^{-1}$. D. S. N. Rupke et al. (2019) have argued that these two wind components were produced by the two distinct bursts of star formation detected in the central core, Episode I (0.4 Gyr ago) and Episode II (7 Myr ago). The Episode II ionized outflow is accompanied by two other gas phases: high-velocity (up to ±1500 km $s^{-1}$) cold molecular gas traced by millimeter-wave CO (2–1) line emission and a cool neutral-atomic gas in the velocity range ±500 km $s^{-1}$ traced by resonant line emission from Mg II 2796, 2803 Å (IP = 8 eV).

The extended PAH and infrared continuum emission shown in Figures 2−4 and Figure 5 traces the distribution of the warm dust across both the inner and outer winds of Makani. The presence of dust in the outer warm ionized wind is unexpected since the optical reddening due to dust, $E(B-V)$, derived by D. S. N. Rupke et al. (2023) from the Keck/Echellette Spectrograph and Imager long-slit measurements of the H$\alpha$/H$\beta$ ratios assuming Case B recombination decreases with radius from a peak value of ∼1 mag at $R$ = 10 kpc to ∼0 mag at $R$ > 25 kpc. Nonzero extinction is measured at the base of this cloud complex (e.g., $E(B-V) = 0.42 \pm 0.06$ mag at $R \sim 21$ kpc in aperture #3 defined[14] in the upper left panel of Figure 6), but not beyond (e.g., in aperture #2 at $R \sim$ 25.5 kpc). We note, however, that the long-slit measurements of D. S. N. Rupke et al. (2023) do not fully sample the NW warm-dust clouds at $R \gtrsim 25$ kpc (e.g., Figure 6), so it is quite possible that the slit missed some of the dust.

The presence of dust in the outer Episode I warm ionized nebula speaks to the durability of dust in the galactic wind environment. The dynamical time of the outflowing dusty gas to reach distances of ∼30 kpc is $t_{\rm dyn} \sim R/V \sim 0.1$ Gyr, assuming that the dust is entrained at the same velocity as the

[14] Note that the aperture definition here is different from that of D. S. N. Rupke et al. (2023).

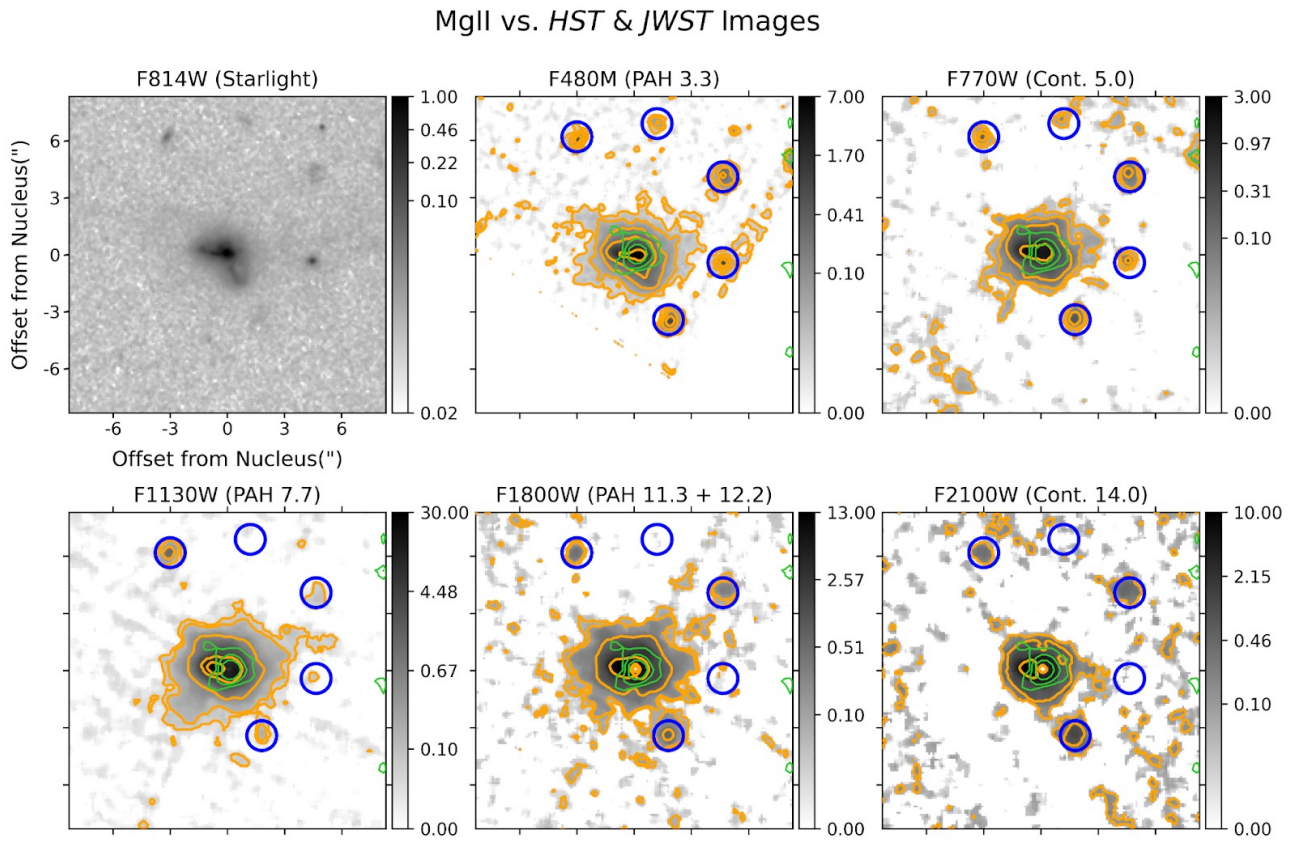


**Figure 3.** Same as Figure 2 but here the green contours show the Mg II 2800 Å line emission instead of CO (2–1). The green contour levels are 0.15, 0.29, and $0.59 \times 10^{-16}$ erg s$^{-1}$ cm$^{-2}$ arcsec$^{-2}$.

gas at an average velocity of 300 km s$^{-1}$. This timescale may be compared with the dust erosion/destruction timescale. Several processes may be at work in the wind, e.g., collisions with other grains (shattering), sputtering due to collisions with ions, sublimation or evaporation, explosion due to UV radiation, and alteration of grain material by cosmic rays and X-rays. The thermal sputtering time of a dust grain of size $a$ in a hot plasma of density $\rho$ and temperature $T$ is approximately given by

$$t_{\rm sp} \approx 0.17\ {\rm Gyr} \left(\frac{a}{0.1\ \mu{\rm m}}\right)\left(\frac{10^{-27}{\rm g\ cm^{-3}}}{\rho}\right) \times \left[\left(\frac{10^{6.3}\ {\rm K}}{T}\right)^{\omega} + 1\right], \quad (1)$$

where $\omega = 2.5$ (J. C. Tsai & W. G. Mathews 1995; H. Hirashita 2015; R. McKinnon et al. 2017; H. M. Richie et al. 2024).

Using the optical line flux ratios [O II] 3729 Å/3726 Å and [S II] 6716 Å/6731 Å, D. S. N. Rupke et al. (2023) derived an upper limit on the electron density $n_{e,\rm warm} \lesssim 10$ cm$^{-3}$ in the warm ionized gas phase ($T \sim 10^4$ K) at the base of the NW dusty clouds entrained in the wind ($R \sim 21$ kpc; aperture #3 in Figure 6 = aperture #5 in the nomenclature of D. S. N. Rupke et al. 2023), corresponding to an upper limit on the mass density of the plasma $\rho_{\rm warm} \lesssim 1 \times 10^{-23}$ g cm$^{-3}$. Assuming pressure equilibrium between the warm and hot gas phases, the electron density in the hot gas phase at $R \sim 20$ kpc is $n_{e,\rm hot} \lesssim 0.1$ cm$^{-3}$, corresponding to $\rho_{\rm hot} \lesssim 1 \times 10^{-25}$ g cm$^{-3}$. Unless this density is highly overestimated (which we consider unlikely; see below), we find $t_{\rm sp} \gtrsim 1$ Myr ($a/0.1\ \mu$m) and therefore expect the dust grains entrained in the wind to be affected by sputtering within the outflow dynamical timescale (~0.1 Gyr). This is especially true for smaller grains such as PAHs where $a = 0.001$–$0.01\ \mu$m (E. R. Micelotta et al. 2010a; H. M. Richie et al. 2024, H. M. Richie & E. E. Schneider 2025), implying $t_{\rm sp} \gtrsim 10^4$–$10^5$ yr.

Note that our estimate of the electron density in the hot gas phase at $R \sim 20$ kpc is an upper limit, so the sputtering time is a lower limit and could therefore, in principle, be comparable to, or even larger than, the dynamical timescale if it is severely overestimated. However, the electron density in the hot phase would have to be overestimated by a factor of $\sim 10^3$–$10^4$ ($n_{e,\rm hot} \sim 10^{-5}$–$10^{-4}$ cm$^{-3}$, corresponding to $n_{e,\rm warm} \sim 10^{-3}$–$10^{-2}$ cm$^{-3}$, assuming thermal equilibrium) for the sputtering time to be comparable to the outflow dynamical timescale at $R \sim 30$ kpc (~0.1 Gyr); this seems unlikely for several reasons.

First, we note that the upper error bar on the electron density measurement of D. S. N. Rupke et al. (2023) is rather large (1.5–2.3 dex) due to the decreasing sensitivity of the optical line ratios to densities below ~50 cm$^{-3}$. The upper limit on the electron density of the warm ionized gas phase at $R \sim 20$ kpc is therefore formally $n_{e,\rm warm} \lesssim 10$–$50$ cm$^{-3}$. For comparison, the electron density of the warm ionized wind within the central aperture of Makani (i.e., the blueshifted component of [O II] with a large velocity dispersion within $R = 0$–$5.5$ kpc) is ~2500 cm$^{-3}$, or ≳50–250× larger than that of the warm ionized wind component at ~20 kpc. This density contrast is larger than that of the warm ionized wind in M82 ($\propto R^{-1.17}$;

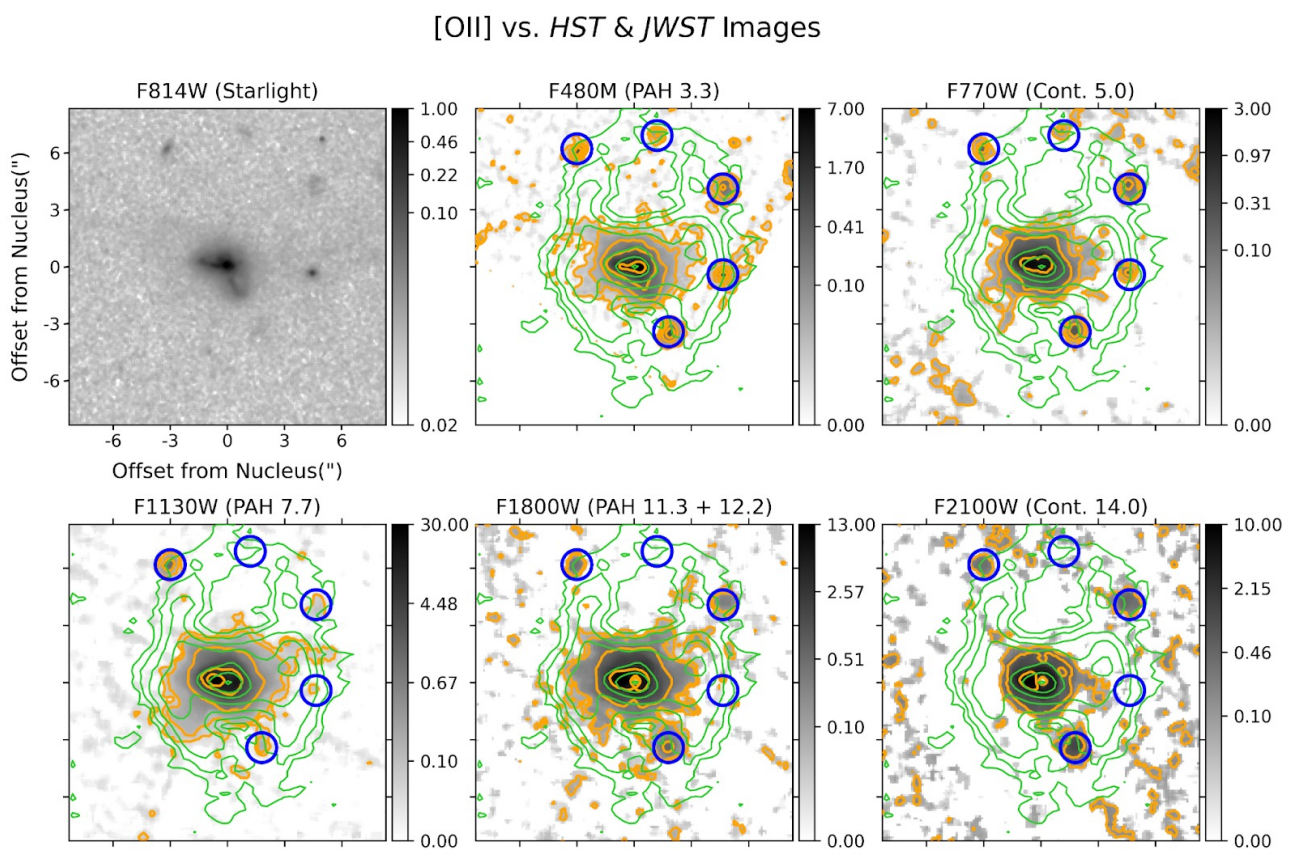


**Figure 4.** Same as Figure 2 but here the green contours show the [O II] 3727 Å line emission instead of CO (2–1). The green contour levels are 0.037, 0.074, 0.15, 0.29, 0.59, 1.2, and 2.4 × $10^{-16}$ erg $s^{-1}$ $cm^{-2}$ $arcsec^{-2}$.

X. Xu et al. 2023), but approximately consistent with adiabatic expansion ($\propto R^{-2}$). A much lower value of $n_{e,\rm warm}$ at $R \sim$ 20 kpc would imply a very steep density gradient of the form $R^{-3}$ or $R^{-4}$, which would be unusual for galactic winds and difficult to explain physically (e.g., S. Veilleux et al. 2005, 2020).

Although there are no direct estimates of the electron density in the hot gas phase of the Makani wind, estimates in the X-ray emitting wind fluid of M82 may be used as a guide. Using deep Chandra data, L. A. Lopez et al. (2020) inferred a flat density profile where $n_{e,\rm hot} \sim 0.01$–$0.03$ $cm^{-3}$ at $R = 1$–$3$ kpc, values that are roughly consistent with our adopted estimate of $n_{e,\rm hot}$ at $R \sim 20$ kpc in Makani. Note, finally, that our estimates of $n_{e,\rm warm}$ and $n_{e,\rm hot}$ in Makani refer to the inner ($R \sim 20$ kpc) CGM, which is mass-loaded by the galactic wind. They should not be compared with the smaller values inferred from refractive fast radio burst scattering measurements ($n_{e,\rm warm} \sim 10^{-3}$–$10^{-1}$ $cm^{-3}$; e.g., L. Mas-Ribas et al. 2025 and references therein), and used in numerical simulations ($n_{e,\rm hot} \sim 10^{-5}$–$10^{-3}$ $cm^{-3}$; see references in J. Tumlinson et al. 2017; C.-A. Faucher-Giguère & S. P. Oh 2023), which typically refer to the CGM at ∼100 kpc. But note that even these small values of $n_{e,\rm warm}$ and $n_{e,\rm hot}$ imply a thermal sputtering timescale for the smallest dust grains that is shorter than, or comparable to, the outflow dynamical timescale (0.1 Gyr).

In summary, thermal sputtering of the small dust grains responsible for the mid-infrared emission detected with JWST is expected to be significant in the dense, inner CGM of Makani. Moreover, other processes such as nonthermal (inertial) sputtering due to the nonzero velocity of the dust grains relative to the gas associated with shocks, known to be present in Makani (D. S. N. Rupke et al. 2023), are expected to further contribute to the dust grain erosion (e.g., C.-Y. Hu et al. 2019). Again, smaller grains such as PAHs are expected to be even more susceptible to destruction by shocks (e.g., E. R. Micelotta et al. 2010b).

Dust destruction may be avoided if the dust is shielded from these processes through cloud–wind mixing and condensation. A (dust-bearing) cool cloud may be able to survive longer than a dynamical time if the cooling time of the mixed layer between the wind and cloud material is shorter than the advection (shear) timescale $t_{\rm shear} = r_{\rm cl}/v_w$, where $r_{\rm cl}$ is the cloud length and $v_w$ is the wind speed (e.g., F. Marinacci et al. 2010; L. Armillotta et al. 2016; M. Gronke & S. P. Oh 2018, 2020; Z. Li et al. 2020; M. Sparre et al. 2020; V. Kanjilal et al. 2021; R. J. Farber & M. Gronke 2022; M. W. Abruzzo et al. 2023). The cloud survival criterion is $t_{\rm cool,minmix} \lesssim 7 t_{\rm shear}$ (M. W. Abruzzo et al. 2023), where the first term is the cooling time at $T = \sqrt{T_{\rm min} T_w}$, where $T_{\rm min}$ is the temperature between the cloud and wind temperatures, $T_{\rm cl}$ and $T_w$, where the cooling time is minimized. In the simulations of H. M. Richie et al. (2024), $T_{\rm min} \sim 3 \times 10^4$ K and the masses of the clouds that meet this criterion grow with time and the dust are able to survive over ∼80 $t_{\rm sp}$, which is similar to the dynamical timescale of the outflow at $R \sim 30$ kpc. This process may therefore help explain both the presence of PAHs within this radius and the absence of significant PAH emission beyond

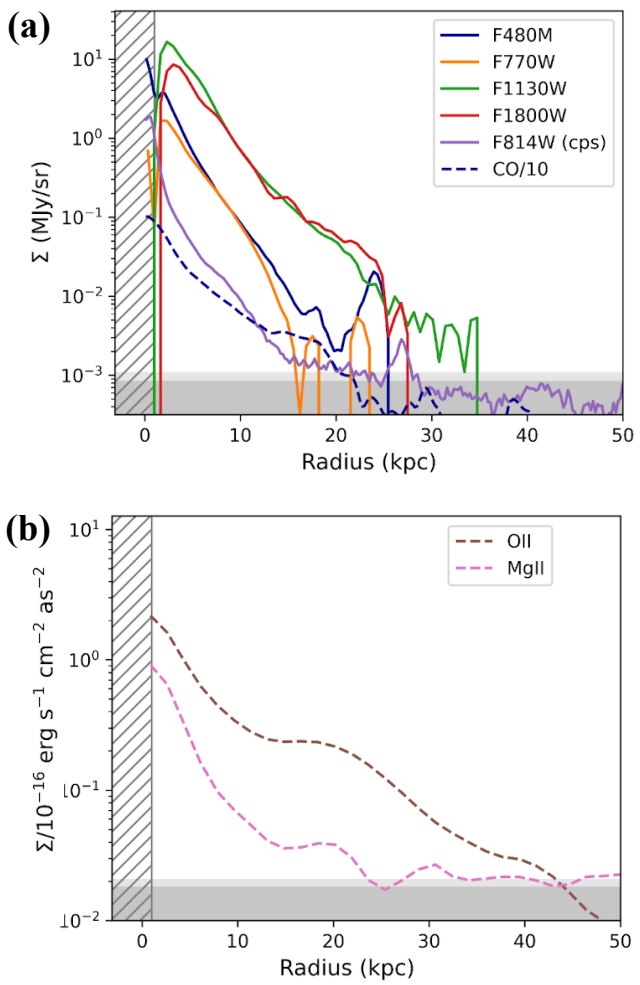


**Figure 5.** (a) Radial surface brightness profiles in the JWST filters (after PSF subtraction with STPSF); the HST F814W filter, which probes starlight near ∼5600 Å; and the line emission in CO (2–1) (within [−500, +500] km s$^{-1}$). (b) Same as (a) but for [O II] 3727 Å and Mg II 2800 Å. Measurements in the vertical hatched region at radii smaller than ∼2 kpc are not shown since they are affected by the PSF subtraction. The horizontal gray areas in (a) and (b) are the detection thresholds of the CO (2–1) and Mg II surface brightness measurements, respectively.

this radius (although we cannot exclude the possibility that the absence of PAH emission at $R \gtrsim 30$ kpc is simply due to the detection limits of the JWST data). A similar argument was recently used to help explain the extent and hourglass morphology of the far-ultraviolet O VI 1032, 1038 Å emission in Makani, which is similar to that of [O II] (T. Ha et al. 2025).

If this scenario is correct, one might expect the cool ($T < 10^4$ K) gas to extend on the same scale as the PAH emission, which at first seems inconsistent with the nondetection of CO (2−1) and Mg II beyond 20 kpc. However, as pointed out in Section 3.3, the F1130W/CO (2−1), F1800W/CO (2−1), F1130W/Mg II, and F1800W/Mg II flux ratios remain relatively constant out to distances of ∼20 kpc from the center, as expected in the scenario where the PAH/CO and Mg II/CO ratios are constant. A constant PAH/CO (1−0) flux ratio was also observed across the inner 2 kpc of the M82 wind by V. Villanueva et al. (2025). The nondetection of CO (2−1) and Mg II beyond 20 kpc in Makani may therefore be due to the shallower detection limits on CO (2–1) and Mg II in the present ALMA and KCWI data, respectively, relative to the JWST detection limits on the PAH emission, rather than the true absence of cool gas at $R \gtrsim 20$ kpc.

**Table 2**
Measured NIRCam and MIRI Flux Densities

| Filters | Main Diagnostics | $f_\nu^{\rm nuc}$ (mJy) | $f_\nu^{\rm inner-halo}$ ($\mu$Jy) | $f_\nu^{\rm CGM-E}$ ($\mu$Jy) | $f_\nu^{\rm CGM-W}$ ($\mu$Jy) |
|---|---|---|---|---|---|
| (1) | (2) | (3) | (4) | (5) | (6) |
| N-F187N | Pa$\beta$ 1.28 | ⋯ | ⋯ | ⋯ | ⋯ |
| N-F480M | PAH 3.3 | 0.19 | 10.6 | $\lesssim$0.4 | $\lesssim$0.3 |
| M-F770W | Continuum (5 $\mu$m) | 0.36 | 8.5 | $\lesssim$0.3 | $\lesssim$0.3 |
| M-F1130W | PAH 7.7 | 2.32 | 95.0 | 3.7 | 3.8 |
| M-F1800W | PAH (11.3 + 12.2) | 3.24 | 78.9 | 2.6 | $\lesssim$0.4 |
| M-F2100W | Continuum (14 $\mu$m) | 3.62 | 2.7 | $\lesssim$0.3 | $\lesssim$0.3 |
| M-F2550W | $H_2$ 17.03 | 5.64 | ⋯ | ⋯ | ⋯ |

**Note.** Meaning of the columns: (1) Name of the NIRCam (N) or MIRI (M) filters. (2) Main diagnostics in the filter bandpass. (3) Flux densities in mJy measured in the unresolved nucleus (i.e., the central PSF); the statistical uncertainties on these measurements are less than 1%. (4) Flux densities in $\mu$Jy of the dust emission in the inner halo within an annular aperture centered on the nucleus with inner and outer radii of 1.″78 and 3″, respectively (see Figure 6 and text for more details); the typical uncertainties on these measurements are ±0.3 $\mu$Jy. (5)–(6) Flux densities in $\mu$Jy of the dust emission in the outer halo within two circular apertures centered on the brighter mid-infrared emission beyond 3″ (see Figure 6 and text for more details); the typical uncertainties on these measurements are ±0.3 $\mu$Jy.

### 4.2. Properties of the Dust in the Galactic Wind

The physical state of dust grains may be assessed from the relative strengths of the PAH features and surrounding continuum (e.g., B. T. Draine et al. 2021; D. Rigopoulou et al. 2021, 2024). If the processes of cloud–wind mixing and condensation are indeed important in the CGM of Makani, the PAH flux ratios may be expected to vary radially as the clouds are entrained in the outflow.

In Figure 7, we show the predicted F1800W/F1130W, F770W/F1130W, and F480M/F1130W flux ratios for the B. T. Draine et al. (2021) library of PAH + dust emission spectra, redshifted to $z = 0.459$, for different starlight intensities ($U$), PAH size distributions ($f_{\rm size}$), and PAH ionization fractions ($f_{\rm ion}$). For each model, the predicted fluxes were calculated using the transmission curves of the NIRCam and MIRI filters (Figure 1) without applying any continuum subtraction. $U$ is defined as the normalized energy density such that identical values of $U$ yield the same temperature of dust grains from heating. The value $U = 1$ refers to the heating that would be produced by the starlight spectrum of the solar neighborhood. The $f_{\rm size}$ parameter describes the distribution of grain sizes comprising the PAH population, and is described by three parameter values—small (sma), standard (std), and large (lrg). Finally, the $f_{\rm ion}$ parameter describes the fraction of ionized PAHs relative to the total population. The B. T. Draine et al. (2021) models explore three values of $f_{\rm ion}$: low (lo), standard (st), and high (hi). For this figure, we use the B. T. Draine et al. (2021) models with the starlight spectrum predicted from the single-age stellar population models of G. Bruzual & S. Charlot (2003) for solar metallicity ($Z = 0.02$) and a stellar age of 10 Myr,

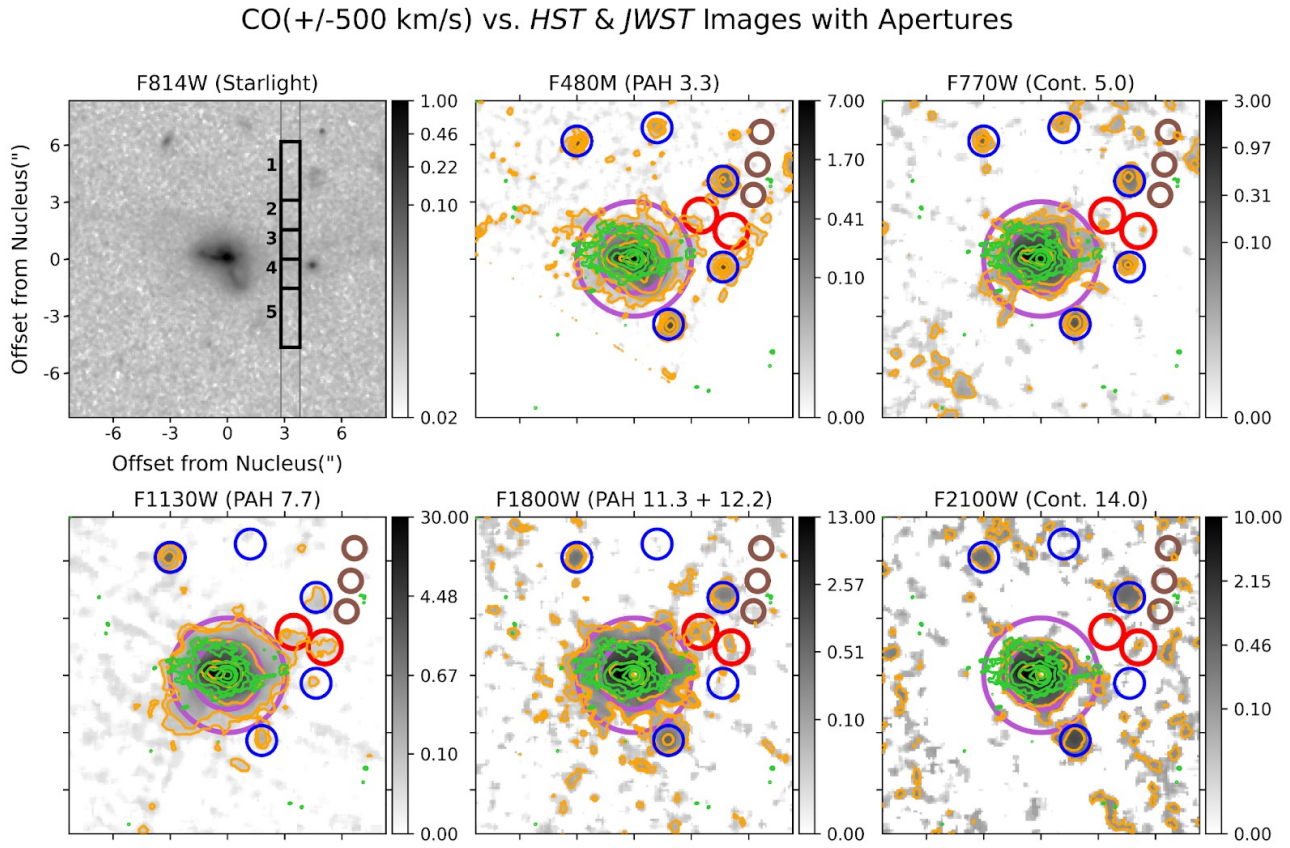


**Figure 6.** Same as Figure 2 but now showing the apertures used to calculate the strength of the dust emission in the inner halo (purple annulus centered on the nucleus with inner and outer radii of 1.″78 and 3″, respectively) and outer halo (CGM-E and CGM-W; eastern and western red circles, respectively). The flux measurements are listed in Table 2. The background level was assessed within the three circular apertures in the upper right corner of each panel, far from any galaxy wind emission. In the upper left panel, we also show the locations of some of the extraction apertures along the Keck/Echellette Spectrograph and Imager long-slit spectrum used by D. S. N. Rupke et al. (2023).

representative of local $L^*$ star-forming galaxies. In S. D. Shockley et al. (2025, in preparation), we show that the flux ratios predicted for other stellar models with either younger stellar age (3 Myr) or lower metallicity ($Z = 0.0004 = 2\%$ solar) lie within 5% of each other.

All three filter flux ratios are sensitive to the starlight intensity, especially for values of log $U$ above 4. F1800W/F1130W and F480M/F1130W also provide some constraints on the PAH size distributions and PAH ionization fractions, especially for small values of log $U$. We compare these predictions with the measured values of these ratios listed in Table 2 for the nucleus (PSF), inner halo (purple annulus at $R \sim 10$–$20$ kpc in Figure 6), and outer halo (red circular apertures in Figure 6 centered on the NW circumgalactic cloud complex at $R \sim 20$–$35$ kpc). In the nucleus, the measured high values of F1800W/F1130W ($\sim$1.4), F480M/F1130W ($\sim$0.07), and F770W/F1130W ($\sim$0.14) all point to large starlight intensities, PAH sizes that are larger than the standard distribution, and small ionization fractions.

In contrast, the smaller values of F1800W/F1130W in both the inner halo ($\sim$0.83) and outer halo ($\sim$0.70) can only be reproduced if the starlight intensity is low (log $U \lesssim 0$), the PAH sizes are smaller than the standard distribution, and the ionization fractions are elevated relative to the standard ionization distribution of B. T. Draine et al. (2021). The upper limits of $\lesssim$0.1 on the F480M/F1130W flux ratios in both the inner and outer halo regions are consistent with these conclusions, but are too high to provide additional physically meaningful constraints. The upper limits on the F770W/F1130W flux ratios in these regions ($\lesssim$0.1) also favor small log $U$ values, but do not constrain the PAH sizes and ionization fractions.

The results of Makani seem qualitatively different from the Spitzer results in M82. The PAH 11.3/7.7 ratios in the northern wind of M82 increase with increasing distance from the midplane, particularly beyond 2 kpc, indicating that the PAH emitters in the wind are more neutral than those in the starburst disk (P. Beirão et al. 2015).[15] Cold clouds in the wind of M82 may not only survive the erosive processes associated with the acceleration by a warm, fast wind, but grow in mass as they flow out, due to radiative cooling in the mixed gas (M. Gronke & S. P. Oh 2018, 2020; E. E. Schneider et al. 2020; W. E. Banda-Barragán et al. 2021) or thermal instabilities in the hot fluid (T. A. Thompson et al. 2016). On the other hand, in Makani, the smaller F1800W/F1130W flux ratios in the inner and outer halos at $r \sim 15$ kpc and $\sim$35 kpc, respectively, relative to the value in the nucleus indicate a radially decreasing PAH (11.3 + 12.2)/7.7 ratio profile. This is due in large part to the radially decreasing starlight intensity. But as discussed above, the actual F1800W/F1130W flux ratios in

[15] Note that the recent JWST analysis of V. Villanueva et al. (2025) covers the region within 2 kpc from the center of M82 so it cannot confirm the results of P. Beirão et al. (2015).

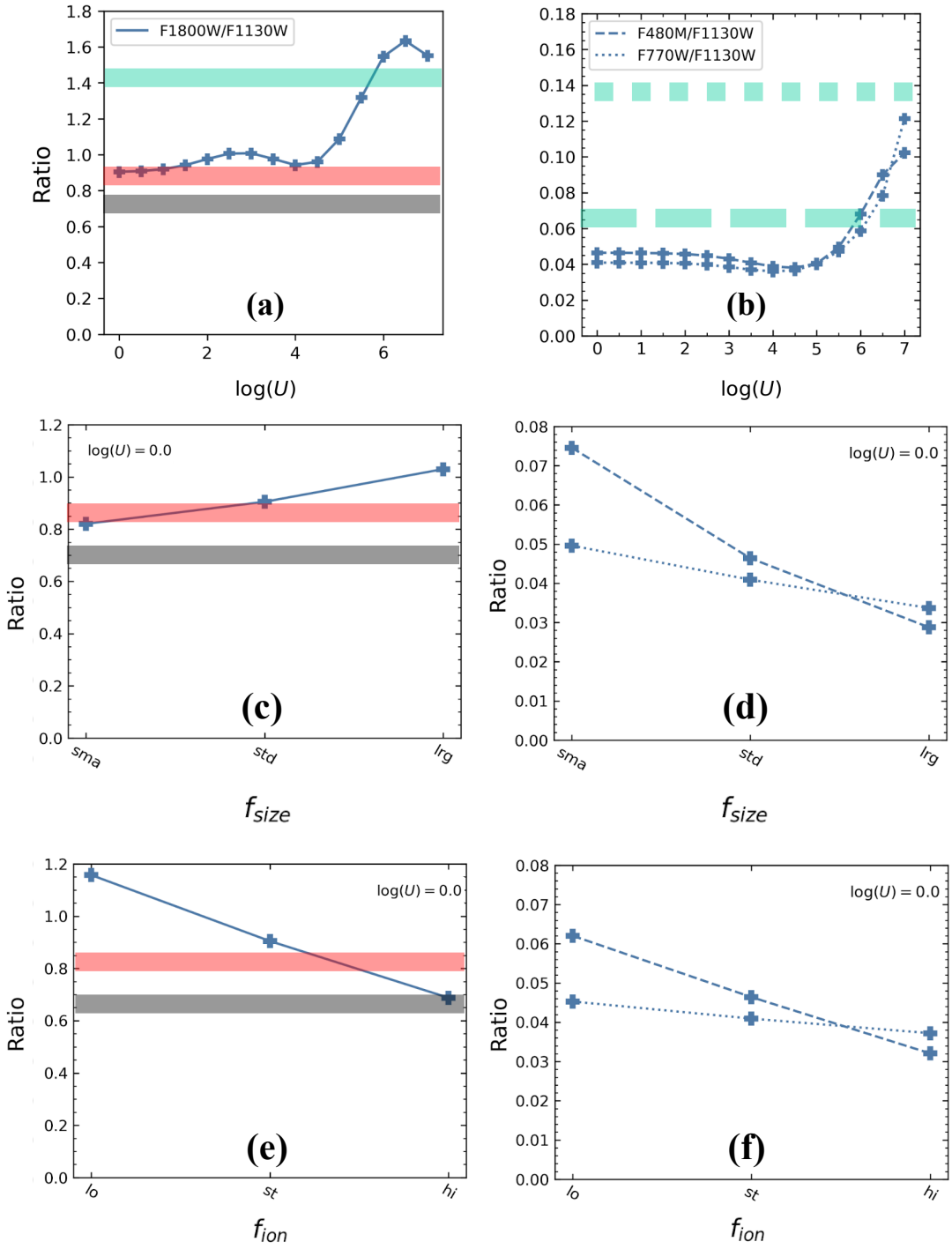


**Figure 7.** Measured and predicted filter flux ratios. The values of F1800W/F1130W are shown in the left panels, while F480M/F1130W and F770W/F1130W are shown in the right panels. The measured values are shown as thick, semitransparent horizontal lines. Their colors refer to the extraction regions (nucleus = cyan, inner halo = red, and outer halo = black), while the line styles refer to the filter flux ratios (F1800W/F1130W = solid line, F480M/F1130W = dashed line, and F770W/F1130W = dotted line). Upper limits on the filter flux ratios are not shown in these panels (see Table 2 and text in Section 4.2). The values predicted by the models of B. T. Draine et al. (2021) are shown as blue curves for different values of the starlight intensities on the dust (log $U$, upper panels), the PAH size distributions ($f_{size}$, middle panels), and the PAH ionization fractions ($f_{ion}$, bottom panels). The results in the upper panels are for a standard PAH size distribution and PAH ionization fraction, while those in the middle and bottom panels are for a fixed value of $\log(U) = 0.0$, which is appropriate for the inner and outer halos, and a standard PAH ionization fraction and PAH size distribution, respectively. See text in Section 4.2 for more details.

the inner and outer halos also imply a reduction of the average PAH sizes and an increase in PAH ionization with increasing radial distances, both pointing to PAH destruction on the journey to the outer halo (e.g., D. Narayanan et al. 2023). The outflow timescale ($R/v$) of Makani is ∼10–100× that of M82, so we may be seeing long-term dust evolution in Makani that is simply not probed by the M82 Spitzer data. This erosion of the dust grains in Makani may also coincide with the dissolution of the outflowing cool clouds into the warm ionized phase, as predicted by theory (e.g., E. Scannapieco &

M. Brüggen 2015; A. Ferrara & E. Scannapieco 2016; D. Decataldo et al. 2017). However, we cannot formally rule out the possibility that both the dust and cool gas survive out to ~35 kpc, and perhaps even beyond, given the detection limits on the cool gas (warm dust) beyond ~20 (35) kpc in the existing ALMA and KCWI (JWST) data (Section 4.1).

## 5. Conclusions

We report the results of our analysis of deep NIRCam and MIRI images centered on the PAH 3.3, 7.7, and (11.3 + 12.2) features and adjacent continuum regions in the Makani Galaxy, a compact poststarburst galaxy ($r_e$ = 2.3 kpc) at $z = 0.459$ with a warm ionized wind that spans 100 kpc. The main conclusions are as follows:

1. A careful removal of the bright central source in this object using STPSF reveals PAH 7.7 and (11.3 + 12.2) emission that extends to ~35 kpc and ~30 kpc, respectively, well beyond the Mg II and CO 2−1 line emission associated with the more recent (7 Myr) starburst episode, but not as far as the outer [O II] line emission produced by the older (0.5 Gyr) episode.
2. The discovery of PAHs in the warm ionized wind indicates that they survive the long journey ($R/v \sim 10^8$ yr) to the CGM. Dust destruction due to thermal sputtering and the many other processes taking place in the harsh environment of the galactic wind may be avoided if the dust is shielded through cloud–wind mixing and condensation. The roughly constant PAH-to-CO and PAH-to-Mg II flux ratios with radial distances from the center are consistent with this scenario. Cool gas may be present beyond 20 kpc, but is beyond the detection limits of the existing ALMA and KCWI data. Similarly, the detection limits of our JWST data may prevent us from detecting warm-dust emission beyond ~35 kpc.
3. The F1800W/F1130W flux ratio, tracer of the PAH (11.3 + 12.2)/7.7 ratio, is smaller in the inner halo at $R$ = 10–20 kpc and outer halo at $R \sim$ 20–35 kpc than in the unresolved nuclear emission, indicating that the PAH emitters in the inner and outer halos are not only more weakly illuminated than those in the nucleus, which is expected, but also smaller and more ionized. This is the first evidence for dust evolution on an outflow dynamical timescale of $\sim 10^8$ yr. This result is qualitatively different from that found in M82, where the PAH (11.3 + 12.2)/7.7 ratio increases over a dynamical timescale of $\sim 10^6$ yr. The measured upper limits on the F480M/F1130W and F770W/F1130W flux ratios, tracers of the PAH 3.3/7.7 and 5 $\mu$m continuum/PAH 7.7 ratios in these regions, are consistent with these radial trends.
4. Overall, these results provide the strongest evidence so far that the ejected dust of galactic winds may survive the long journey to the CGM, but erodes along the way.

## Acknowledgments

We thank the anonymous referee for constructive comments that helped improve this paper. This work is based [in part] on observations made with the NASA/ESA/CSA James Webb Space Telescope. These observations are associated with program #1865. The JWST data presented in this article were obtained from the Mikulski Archive for Space Telescopes (MAST) at the Space Telescope Science Institute. The specific observations analyzed can be accessed via doi:10.17909/1r37-nb46. Support for program #1865 was provided by NASA through a grant from the Space Telescope Science Institute, which is operated by the Association of Universities for Research in Astronomy, Inc., under NASA contract NAS 5-03127.

*Facilities:* JWST (MIRI, NIRCam).

*Software:* astropy (Astropy Collaboration et al. 2013, 2018), STPSF (M. D. Perrin et al. 2014).

## Author Contributions

S.V. conceived and led the implementation of the JWST program, helped with the data analysis, led the interpretation of the data, and wrote the manuscript. S.D.S. produced the figures and led the comparison of the measured filter flux ratios with the predicted values of the PAH + dust models. M.M. carried out the STPSF analysis and edited the manuscript. D.S.N.R. helped with the analysis and figures and edited the JWST proposal and manuscript. C.A.T. and H.C. provided the nuclear spectrum shown in Figure 1 and edited the JWST proposal and manuscript. A.L.C., A.M.D.-S., J.E.G., R.C.H., J.M., G.H.R., and P.H.S. helped improve the JWST proposal and manuscript.

## ORCID iDs

Sylvain Veilleux https://orcid.org/0000-0002-3158-6820
Marcio Meléndez https://orcid.org/0000-0001-8485-0325
David S. N. Rupke https://orcid.org/0000-0002-1608-7564
Alison L. Coil https://orcid.org/0000-0002-2583-5894
James E. Geach https://orcid.org/0000-0003-4964-4635
Ryan C. Hickox https://orcid.org/0000-0003-1468-9526
John Moustakas https://orcid.org/0000-0002-2733-4559
Gregory H. Rudnick https://orcid.org/0000-0001-5851-1856
Paul H. Sell https://orcid.org/0000-0003-1771-5531
Christy A. Tremonti https://orcid.org/0000-0003-3097-5178

## References

Abruzzo, M. W., Fielding, D. B., & Bryan, G. L. 2023, arXiv:2307.03228
Armillotta, L., Fraternali, F., & Marinacci, F. 2016, MNRAS, 462, 4157
Astropy Collaboration, Price-Whelan, A. M., Sipőcz, B. M., et al. 2018, AJ, 156, 123
Astropy Collaboration, Robitaille, T. P., Tollerud, E. J., et al. 2013, A&A, 558, A33
Banda-Barragán, W. E., Brüggen, M., Heesen, V., et al. 2021, MNRAS, 506, 5658
Beirão, P., Armus, L., Lehnert, M. D., et al. 2015, MNRAS, 451, 2640
Biernacki, P., & Teyssier, R. 2018, MNRAS, 475, 5688
Bolatto, A. D., Levy, R. C., Tarantino, E., et al. 2024, ApJ, 967, 63
Brennan, R., Choi, E., Somerville, R. S., et al. 2018, ApJ, 860, 14
Bruzual, G., & Charlot, S. 2003, MNRAS, 344, 1000
Choi, E., Somerville, R. S., Ostriker, J. P., Naab, T., & Hirschmann, M. 2018, ApJ, 866, 91
Davé, R., Anglés-Alcázar, D., Narayanan, D., et al. 2019, MNRAS, 486, 2827
Decataldo, D., Ferrara, A., Pallottini, A., Gallerani, S., & Vallini, L. 2017, MNRAS, 471, 4476
Draine, B. T., Li, A., Hensley, B. S., et al. 2021, ApJ, 917, 3
Dubois, Y., Peirani, S., Pichon, C., et al. 2016, MNRAS, 463, 3948
Farber, R. J., & Gronke, M. 2022, MNRAS, 510, 551
Faucher-Giguère, C.-A., & Oh, S. P. 2023, ARA&A, 61, 131
Ferrara, A., & Scannapieco, E. 2016, ApJ, 833, 46

Fisher, D. B., Bolatto, A. D., Chisholm, J., et al. 2025, MNRAS, 538, 3068
Gardner, J. P., Mather, J. C., Abbott, R., et al. 2023, PASP, 135, 068001
Gronke, M., & Oh, S. P. 2018, MNRAS, 480, L111
Gronke, M., & Oh, S. P. 2020, MNRAS, 492, 1970
Ha, T., Rupke, D. S. N., Caraker, S., et al. 2025, ApJ, 986, 87
Hafen, Z., Faucher-Giguère, C.-A., Anglés-Alcázar, D., et al. 2019, MNRAS, 488, 1248
Hirashita, H. 2015, MNRAS, 447, 2937
Hopkins, P. F., Wetzel, A., Kereš, D., et al. 2018, MNRAS, 480, 800
Hu, C.-Y., Zhukovska, S., Somerville, R. S., & Naab, T. 2019, MNRAS, 487, 3252
Kanjilal, V., Dutta, A., & Sharma, P. 2021, MNRAS, 501, 1143
Li, Z., Hopkins, P. F., Squire, J., & Hummels, C. 2020, MNRAS, 492, 1841
Lopez, L. A., Mathur, S., Nguyen, D. D., Thompson, T. A., & Olivier, G. M. 2020, ApJ, 904, 152
Marinacci, F., Binney, J., Fraternali, F., et al. 2010, MNRAS, 404, 1464
Mas-Ribas, L., McQuinn, M., & Prochaska, J. X. 2025, arXiv:2504.19562
McCleary, J. E., Huff, E. M., Bartlett, J. W., & Hensley, B. S. 2025, arXiv:2503.04098
McKinnon, R., Torrey, P., Vogelsberger, M., Hayward, C. C., & Marinacci, F. 2017, MNRAS, 468, 1505
Ménard, B., Scranton, R., Fukugita, M., & Richards, G. 2010, MNRAS, 405, 1025
Micelotta, E. R., Jones, A. P., & Tielens, A. G. G. M. 2010a, A&A, 510, A37
Micelotta, E. R., Jones, A. P., & Tielens, A. G. G. M. 2010b, A&A, 510, A36
Narayanan, D., Smith, J. D. T., Hensley, B. S., et al. 2023, ApJ, 951, 100
Nelson, D., Pillepich, A., Springel, V., et al. 2019, MNRAS, 490, 3234
Peek, J. E. G., Ménard, B., & Corrales, L. 2015, ApJ, 813, 7
Peeples, M. S., Corlies, L., Tumlinson, J., et al. 2019, ApJ, 873, 129
Perrin, M. D., Sivaramakrishnan, A., Lajoie, C.-P., et al. 2014, Proc. SPIE, 9143, 91433X
Planck Collaboration, Aghanim, N., Akrami, Y., et al. 2020, A&A, 641, A6
Richie, H. M., & Schneider, E. E. 2025, ApJ, submitted (arXiv:2505.11734)
Richie, H. M., Schneider, E. E., Abruzzo, M. W., & Torrey, P. 2024, ApJ, 974, 81
Rigby, J., Perrin, M., McElwain, M., et al. 2023, PASP, 135, 048001
Rigopoulou, D., Barale, M., Clary, D. C., et al. 2021, MNRAS, 504, 5287
Rigopoulou, D., Donnan, F. R., Garcìa-Bernete, I., et al. 2024, MNRAS, 532, 1598
Rupke, D. S. N., Coil, A., Geach, J. E., et al. 2019, Natur, 574, 643
Rupke, D. S. N., Coil, A. L., Perrotta, S., et al. 2023, ApJ, 947, 33
Scannapieco, E., & Brüggen, M. 2015, ApJ, 805, 158
Schaye, J., Crain, R. A., Bower, R. G., et al. 2015, MNRAS, 446, 521
Schneider, E. E., Ostriker, E. C., Robertson, B. E., & Thompson, T. A. 2020, ApJ, 895, 43
Sell, P. H., Tremonti, C. A., Hickox, R. C., et al. 2014, MNRAS, 441, 3417
Sparre, M., Pfrommer, C., & Ehlert, K. 2020, MNRAS, 499, 4261
Thompson, T. A., Quataert, E., Zhang, D., & Weinberg, D. H. 2016, MNRAS, 455, 1830
Tsai, J. C., & Mathews, W. G. 1995, ApJ, 448, 84
Tumlinson, J., Peeples, M. S., & Werk, J. K. 2017, ARA&A, 55, 389
Veilleux, S., Cecil, G., & Bland-Hawthorn, J. 2005, ARA&A, 43, 769
Veilleux, S., Maiolino, R., Bolatto, A. D., & Aalto, S. 2020, A&ARv, 28, 2
Villanueva, V., Bolatto, A. D., Herrera-Camus, R., et al. 2025, A&A, 695, A202
Vogelsberger, M., Genel, S., Springel, V., et al. 2014, MNRAS, 444, 1518
Xu, X., Heckman, T., Yoshida, M., Henry, A., & Ohyama, Y. 2023, ApJ, 956, 142